Heriot-Watt University

Depolarization of rotational angular momentum in CN(A², v = 4) + Ar collisions

McGurk, Stephen; McKendrick, Kenneth George; Costen, Matthew Lawrence; Bennett, Doran; Kos, Jacek; Alexander, M. H.; Dagdigian, P. J.

Link to publication in Heriot-Watt Research Gateway

S. J. McGurk, K. G. McKendrick, M. L. Costen, D. I. G. Bennett, J. Kos, M. H. Alexander, and P. J. Dagdigian

Articles you may be interested in

Parity-dependent oscillations in collisional polarization transfer: CN(A 2, v = 4) + Ar
J. Chem. Phys. **139**, 124304 (2013); 10.1063/1.4821602

Collisional angular momentum depolarization of OH(A) and NO(A) by Ar: A comparison of mechanisms
J. Chem. Phys. **135**, 084306 (2011); 10.1063/1.3625638

Dependence of elastic depolarization cross sections on the potential: OH (X   2) - Ar and NO (X   2) - Ar
J. Chem. Phys. **130**, 204304 (2009); 10.1063/1.3139522

Fine-structure state resolved rotationally inelastic collisions of CH (A 2 ,v=0) with Ar: A combined experimental and theoretical study
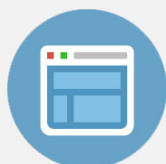J. Chem. Phys. **114**, 4479 (2001); 10.1063/1.1346642

Experimental and theoretical study of rotationally inelastic collisions of highly rotationally excited CN (A 2) with Ar
J. Chem. Phys. **112**, 4474 (2000); 10.1063/1.481010

Depolarization of rotational angular momentum in CN(A²Π, v = 4) + Ar collisions

S. J. McGurk,[1] K. G. McKendrick,[1] M. L. Costen,[1,a)] D. I. G. Bennett,[2,b)] J. Kłos,[2] M. H. Alexander,[2] and P. J. Dagdigian[3,c)]

[1]*School of Engineering and Physical Sciences, Heriot-Watt University, Edinburgh EH14 4AS, United Kingdom*
[2]*Department of Chemistry and Biochemistry and Institute for Physical Science and Technology, University of Maryland, College Park, Maryland 20742-2021, USA*
[3]*Department of Chemistry, The Johns Hopkins University, Baltimore, Maryland 21218-2685, USA*

Angular momentum depolarization and population transfer in CN(A²Π, v = 4, j, F_1e) + Ar collisions have been investigated both experimentally and theoretically. Ground-state CN(X²Σ⁺) molecules were generated by pulsed 266-nm laser photolysis of ICN in a thermal (nominally 298 K) bath of the Ar collision partner at a range of pressures. The translationally thermalized CN(X) radicals were optically pumped to selected unique CN(A²Π, v = 4, j = 2.5, 3.5, 6.5, 11.5, 13.5, and 18.5, F_1e) levels on the A-X (4,0) band by a pulsed tunable dye laser. The prepared level was monitored in a collinear geometry by cw frequency-modulated (FM) spectroscopy in stimulated emission on the CN(A-X) (4,2) band. The FM lineshapes for co- and counter-rotating circular pump and probe polarizations were analyzed to extract the time dependence of the population and (to a good approximation) orientation (tensor rank $K = 1$ polarization). The corresponding parallel and perpendicular linear polarizations yielded population and alignment ($K = 2$). The combined population and polarization measurements at each Ar pressure were fitted to a 3-level kinetic model, the minimum complexity necessary to reproduce the qualitative features of the data. Rate constants were extracted for the total loss of population and of elastic depolarization of ranks $K = 1$ and 2. Elastic depolarization is concluded to be a relatively minor process in this system. Complementary full quantum scattering (QS) calculations were carried out on the best previous and a new set of *ab initio* potential energy surfaces for CN(A)–Ar. Collision-energy-dependent elastic tensor and depolarization cross sections for ranks $K = 1$ and 2 were computed for CN(A²Π, v = 4, j = 1.5–10.5, F_1e) rotational/fine-structure levels. In addition, integral cross sections for rotationally inelastic transitions out of these levels were computed and summed to yield total population transfer cross sections. These quantities were integrated over a thermal collision-energy distribution to yield the corresponding rate constants. A complete master-equation simulation using the QS results for the selected initial level $j = 6.5$ gave close, but not perfect, agreement with the near-exponential experimental population decays, and successfully reproduced the observed multimodal character of the polarization decays. On average, the QS population removal rate constants were consistently 10%–15% higher than those derived from the 3-level fit to the experimental data. The QS and experimental depolarization rate constants agree within the experimental uncertainties at low j, but the QS predictions decline more rapidly with j than the observations. In addition to providing a sensitive test of the achievable level of agreement between state-of-the art experiment and theory, these results highlight the importance of multiple collisions in contributing to phenomenological depolarization using any method sensitive to both polarized and unpolarized molecules in the observed level. © *2012 American Institute of Physics.* [http://dx.doi.org/10.1063/1.4705118]

I. INTRODUCTION

The transfer of energy between translational, rotational, and other degrees of freedom of small molecules is a ubiquitous and important process across the whole range of gas-phase environments, and as such has been the subject of extensive experimental and theoretical investigation. Molecular radicals are of particular interest, as they are important drivers of the chemistry of a wide range of practically significant environments, e.g., combustion, plasmas, the atmosphere, and astrophysical systems. In addition, the open-shell electronic structure and the associated rotational fine-structure give rise to additional dynamical complexity. In the case of collisions with the rare gases, accurate *ab initio* potential energy surfaces (PESs) may be generated, upon which exact quantum scattering (QS) calculations may then be performed. Experimental measurements of the dynamics of these collisions therefore provide a sensitive test of the accuracy of such state-of-the-art calculations.[1,2]

a)Electronic mail: m.l.costen@hw.ac.uk.
b)Present address: Department of Chemistry, University of California, Berkeley, California 94720, USA.
c)Electronic mail: pjdagdigian@jhu.edu.

In general, experimental measurements of inelastic scattering have tended to fall in two categories. In the first, optical double resonance techniques have been used to measure state-to-state population transfer kinetics under thermal collision conditions, for example, rotational energy transfer (RET) rate constants. In the second, crossed-molecular beam methods have been used to measure state-to-state collision cross sections and differential scattering cross sections.[2,3] The latter technique in particular is a very strong test of any calculated PES, but in both cases it is the repulsive regions of the PES that are mostly responsible for the observed scattering. The weaker, longer range, attractive regions of the PES are harder to test experimentally, as collisions that probe these regions are largely elastic in rotational level, and the products are hence challenging to separate from those molecules that have not undergone any collision. However, these rotationally elastic collisions may result in changes in magnetic sub-level, m, classically a re-orientation of the plane of rotation. By preparing the sample in a known spectroscopic level, with angular momentum j, with a known (or measurable) anisotropic polarization, these weak attractive interactions may be studied by observing the collisional removal of the initial polarization, a process termed *elastic depolarization*.[4,5]

A variety of studies in the earlier literature described such measurements, in particular using resolution of the polarization of fluorescence,[6,7] or double resonance optical techniques.[8–11] However, of most relevance here is the recent renaissance of depolarization measurements, with the development by the Edinburgh authors of the Polarization Spectroscopy (PS) technique[12–14] and the simultaneous development of Zeeman Quantum Beat Spectroscopy by Brouard and co-workers.[15] These have been applied in a complementary fashion to the $OH(X^2\Pi/A^2\Sigma^+)$ + Rg (as an example of the collisions of a light rotor) systems,[16–22] and $NO(X^2\Pi/A^2\Sigma^+)$ + Rg (as a heavy rotor) systems.[23,24] Simultaneously, theoretical developments have led to a clear link between the experimental measurements and the quantities that may be calculated by quasi-classical trajectory[25] or QS methods,[26] enabling direct comparison of experimental results and the theoretical predictions.[27–30]

It would be valuable to extend these measurements and calculations to other similar open-shell systems. The $CN(A^2\Pi)$ radical is an excellent candidate for such a study, as it is both experimentally and theoretically tractable, as well as having practical importance in the same gas-phase environments as OH and NO. The inelastic collision dynamics of the $CN(A^2\Pi)$ + Ar system have been the subject of several previous experimental and theoretical investigations, of which the most relevant to the current work are those of Dagdigian and co-workers.[31–33] The experiments measured state-to-state population transfer relative rate constants at a fully state resolved ($jF\varepsilon \rightarrow j'F'\varepsilon'$) level, in the v = 3 vibrational state, for both highly rotationally excited levels (e.g., $N = 60$) and levels near the peak of the room temperature Boltzmann distribution (e.g., $j = 6.5\ F_1e$). The results were compared to QS calculations on *ab initio* PESs, displaying generally good qualitative agreement, suggesting that the repulsive core of the PESs is accurate. The PESs have also been tested by the alternative technique of spectroscopy of the CN(X,A)-Ar van

der Waals complex and its predissociation dynamics. These experiments confirmed that the general form of the PESs was correct, but suggested a dissociation energy for $CN(A^2\Pi$, v = 3)-Ar of 125 cm^{-1},[34] substantially deeper than the 75 cm^{-1} well-depth of the calculated PESs.[33] Subsequent empirical scaling of the PESs to reproduce the observed spectroscopy gave a well-depth of 138 cm^{-1}.[35] This suggests that the attractive regions of the PESs, which we expect to be probed by elastic depolarizing collisions, are substantially deeper than those previously published.[33]

In addition to the PS technique, the Edinburgh authors have also demonstrated the application of double resonance spectroscopy using frequency-modulated (FM) narrow-band cw probe lasers for RET and depolarization studies.[36–39] The FM technique provides sufficient sensitivity to measure population and polarization kinetics of fully state-selected radicals with ns-time resolution and full Doppler discrimination. As well as population and polarization loss in the prepared level, this also includes state-to-state population transfer rate constants, and the associated retention of alignment, as characterized by the multipole transfer efficiency (MTE).[4,40] We used this approach to study the kinetics of population removal and alignment depolarization in collisions with Ar of a range of rotational levels in the $CN(A^2\Pi$, v = 4, j, F_1e) manifold.[39] This study reported rapid alignment depolarization of the initially prepared level, with rate constants for $j = 1.5$–6.5 lying in the range $(1–2) \times 10^{-10}$ cm^3 s^{-1}, surprising for a system with a relatively heavy rotor and modest attractive forces.[5] In contrast, the recent calculations and experiments on the kinematically and electronically very similar $NO(X^2\Pi)$ + Ar system suggest much slower elastic depolarization rate constants, in the range $(0.2–0.4) \times 10^{-10}$ cm^3 s^{-1} across the same range of j.[23]

In this paper, we present new experimental measurements of population removal and the collisional depolarization of both orientation and alignment for $CN(A^2\Pi$, v = 4, j, F_1e) + Ar. In addition, we also report quantum scattering calculations, on new *ab initio* PESs, of the population and polarization kinetics. These QS results are used in master equation modeling of population removal and depolarization, the results of which are compared to the experimental measurements. Finally, we introduce a multi-level scheme for population and polarization kinetics which is of the minimum complexity necessary to fit the experimental data, and hence derive experimental population removal and elastic depolarization rate constants for comparison to the theoretical predictions.

II. METHODOLOGY

A. Experimental

The experimental apparatus has been described in detail previously[36–39] and only the essential details and modifications are described here. These changes increased the temporal resolution of the experiment over those previously reported, and enabled the use of circular polarization in the pump and probe beams. The experiments were performed in a 2 m longitudinal vacuum chamber, evacuated by a

rotary-backed diffusion pump. A cylinder of μ-metal shielding was placed within the vacuum chamber around the beam path to isolate the sample from any stray magnetic fields.[41]

ICN vapor was picked up by a slow flow of Ar (research grade, BOC) controlled via a 10 sccm mass-flow controller (Aera), and passed to the vacuum chamber, where the diffusion pump was throttled to provide ≤ 5 mTorr of ICN in ≈ 30 mTorr of Ar. The desired total pressure of 100–1500 mTorr was attained by addition of a separate flow of Ar through a 100 sccm mass-flow controller (MKS Instruments). The pressure was monitored using a 0–10 Torr capacitance manometer (MKS Instruments).

The ICN was photolyzed by a single pass of a 266-nm beam from a Nd:YAG laser (Continuum Surelite III-10) to produce CN($X^2\Sigma^+$, v = 0) with a near mono-energetic speed distribution in a range of rotational states. A post-photolysis delay of 30 μs ensured essentially complete thermalization of the translational energy distribution, and substantial thermalization of the rotational distribution, and, significantly, ensured that the strong rotational alignment of CN(X) produced in this photolysis was destroyed.[38, 42, 43]

The beam from a Nd:YAG pumped dye laser (Spectron SL803/SL4000) was co-propagated along the photolysis beam with a single pass at a small crossing angle. This pump beam was tuned to selected lines of the R_1 rotational branch of the CN $A^2\Pi$ –$X^2\Sigma^+$ (4,0) band at around 620 nm, and excited the CN to specific $A^2\Pi$(v = 4, j, $F_1 e$) levels. The typical pump laser fluence was ≈ 65 mJ cm^{-2}, strongly saturating but chosen to optimize the tradeoff between excited population and the magnitude of the prepared rotational anisotropy. The pump beam polarization was controlled by a photo-elastic modulator (PEM-80, Hinds Inc.) directly before the entrance to the vacuum chamber. Depending on the retardation applied by the PEM, and the timing of the pump laser pulse relative to the PEM compression cycle, the pump beam could be switched either between horizontal and vertical linear polarization, or alternatively between left and right circular polarization, as confirmed by measurements of the polarization state before and after the chamber. This timing was controlled by a digital delay generator (SRS DG535), under experimental software control.

The prepared CN($A^2\Pi$) molecules were probed by FM stimulated emission using an external cavity tunable diode laser (Sacher GmbH, TEC520) on selected R_1 rotational transitions of the $A^2\Pi$–$X^2\Sigma^+$ (4,2) band between 820 and 835 nm. Note that although the probe is in *stimulated emission*, we have retained the nomenclature of absorption here, for consistency with the spectroscopy in the pump step. The probe beam was frequency modulated at 400 MHz by a broadband phase modulator (Quantum Technology, TWAP-10), driven by a radio frequency generator (Thurlby Thandar, TGR1040). The in-going probe beam counter-propagated the photolysis and pump beams at a small angle and was retro-reflected along a near identical return path. It subsequently exited the chamber via the entry window and was separated from the in-going beam by a pick-off mirror. It was then directed onto a 1 GHz photo-receiver (New Focus, 1601FS-AC) and the 400 MHz FM beat signal sent to the RF arm of an I & Q demodulator (Pulsar Microwave, ID-10-412). The probe
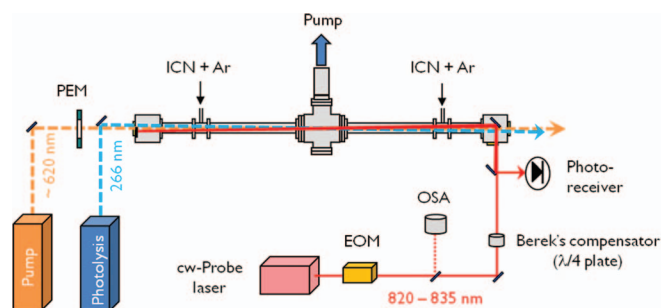

FIG. 1. The FMS experimental setup. PEM, photo-elastic modulator; EOM, electro-optic (phase) modulator; and OSA, optical spectrum analyzer. The Berek's compensator was only included for the orientation experiments.

laser beam was scanned across the transition of interest in 100 MHz increments. The transient in-phase (I) and quadrature (Q) signals were independently averaged over typically 30 photolysis and pump laser shots at each probe laser wavelength using a digital storage oscilloscope (LeCroy LT342). A scanning Fabry-Perot interferometer (CVI Technical Optics, free spectral range 2 GHz) was used to monitor the modulated diode beam, and the output was recorded and subsequently used to linearize the frequency scale of the recorded spectra. The experimental setup-up is summarized in Fig. 1.

Two separate sets of experiments were performed. In *alignment* measurements, the pump laser polarization was switched between vertical and horizontal in the laboratory frame, while the probe beam polarization was fixed as vertical. This gives two geometries we refer to as *parallel* ($\parallel$) and *perpendicular* ($\perp$), respectively. In *orientation* measurements, the probe beam was circularly polarized by a Berek's compensator (New Focus) acting as a $\lambda/4$ plate. This was positioned immediately before the entrance window to the vacuum chamber, and adjusted as necessary to balance any retardance introduced by the reflection of the probe beam from the in-chamber mirrors. The pump laser polarization was then switched between left- and right-handed circular. This gives two geometries that we refer to as *co-rotating* (co) and *counter-rotating* (con), respectively.

The photolysis of ICN at 266 nm produces a small fraction of the CN($X^2\Sigma^+$) in v = 2.[44] This provides an unwanted background absorption signal underneath the CN($A^2\Pi$) stimulated emission signal. Additional background time-traces were therefore acquired at each wavelength step and for each polarization in the absence of the pump pulse. Hence, at each probe wavelength step, four experimental time-traces were acquired sequentially: pump-induced signal and then background for the first geometry; followed by pump-induced signal and then background for the second geometry.

B. Calculation of interaction potential

The PESs are functions of the Jacobi coordinates describing the triatomic system: r (the CN bond distance), R (the distance between the Ar atom and the CN center of mass), and θ (the angle between r and R, with $\theta = 0°$ corresponding to a linear ArNC arrangement). *Ab initio* calculations were carried out for 66 values of R, ranging from 4.9 to 23 bohr with a

denser grid around the van der Waals minima, and a 30° grid in θ spanning 0°–180°. The interatomic distance r of the CN molecule was varied between 2.12 and 2.42 bohr.

We employed an atom-centered avqz atomic-orbital basis,[45,46] with the addition of 3s3p2d2f1g bond functions, with exponents sp, 0.9, 0.3, 0.1; df, 0.6, 0.2; and g, 0.3 placed in the middle of the Jacobi vector $\boldsymbol{R}$.[47] We used the restricted Hartree-Fock (RHF) method to generate reference wave functions for the $CN(X^2\Sigma^+)$–Ar and $CN(A^2\Pi)$–Ar states. With the approach of the Ar atom, the symmetry of the Π state is lowered, resulting in two states of A' and A'' reflection symmetry.[48] The reference wave function for the $CN(A^2\Pi)$–Ar A' adiabatic state was obtained by rotation of the HOMO orbital of the $CN(X^2\Sigma^+)$–Ar state to obtain the proper occupation pattern corresponding to the A state. To account for the electronic correlation energy of each state, the reference wave functions were used as starting points for spin-unrestricted coupled-cluster calculations with single, double, and non-iterative triple excitations [UCCSD(T)].[49] Using this ansatz, 3D PESs could be calculated for both ground and electronically excited CN–Ar complexes. All calculations were carried out with the MOLPRO 2006.3 suite of programs.[50] We kept the default core orbitals set by the program. A counterpoise correction was used at all geometries to correct for basis-set superposition error.[51]

To account for the dependence upon r, we evaluated the PESs at the average of the CN bond length for the $v_A = 4$ vibrational level, namely $\langle r \rangle_{A,v=4} = 2.42$ bohr. Following the work of Alexander describing the interaction of a molecule in a $^2\Pi$ electronic state with a spherical target,[48] we fit the average and half-difference of the PESs corresponding to the states of A' and A'' symmetry:

$$V_{sum}(R,\theta) = \frac{1}{2}\left[V_{A''}(R,\theta) + V_{A'}(R,\theta)\right],$$

$$V_{diff}(R,\theta) = \frac{1}{2}\left[V_{A''}(R,\theta) - V_{A'}(R,\theta)\right]. \quad (1)$$

In the fitting, we used the reproducing kernel Hilbert space method[52,53] to construct an analytic representation of the V_{sum} and V_{diff} hypersurfaces. We construct the necessary 3D kernel spanning separately both radial and angular coordinates.

Figure 2 displays contour plots of the V_{sum} and V_{diff} PESs for the interaction of $CN(A^2\Pi, v = 4)$ with Ar. These plots can be compared with those for the $CN(A^2\Pi, v = 3)$–Ar PESs previously computed by Berning and Werner (B-W).[32] The well in V_{sum} is significantly deeper in the present calculation than in the potential computed previously. For reference, contour plots of V_{sum} and V_{diff} of the B-W potential, as well as the angular expansion coefficients for the present and the B-W PESs, are provided in the supplementary material.[54] It should be noted that the B-W PESs apply to $CN(A^2\Pi, v = 3)$, while the present study pertains to $CN(A^2\Pi, v = 4)$. Only a very slight difference in the PESs is expected for the two vibrational levels.

The dissociation energy D_0 has been computed for both potentials through a variational calculation using the distributed Gaussian method of Hamilton and Light.[55] We obtain $D_0 = 110.0$ and 65.5 cm^{-1} for the present potential and
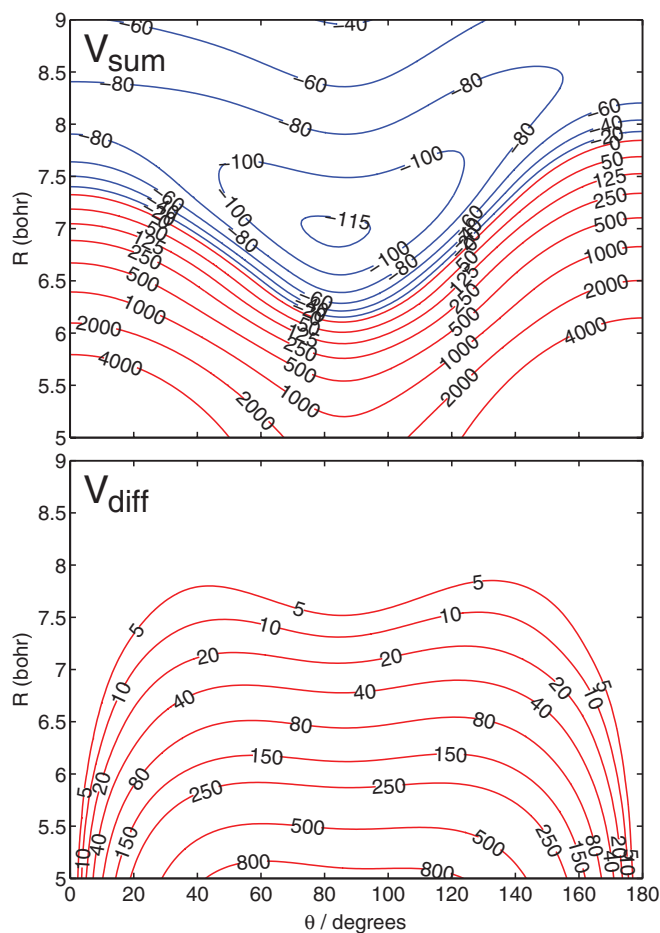

FIG. 2. Contour plots of the potentials V_{sum} (top panel) and V_{diff} (bottom panel) of the PESs for the interaction of $CN(A^2\Pi, v = 4)$ with Ar computed in this work. Contours are labeled in units of cm^{-1}.

the B-W potential,[32] respectively. The former compares favorably with the experimentally determined[34] value $D_0 = 125 \pm 2$ cm^{-1}. Unfortunately, rotational constants are not available for $CN(A^2\Pi)$–Ar van der Waals complexes so that the range of the computed potential cannot be tested by comparison with experimental data.

C. Quantum scattering calculations

Detailed discussion of the collisional evolution of state multipoles, in particular the collisional loss of initially prepared polarization in a specific rotational level, has been given previously.[4,25,26] A brief description of this theory with relevance to rotationally inelastic collisions of an open-shell diatomic molecule is outlined here.

The state multipoles of a rotational level evolve independently of each other in an isotropic distribution of relative velocity vectors, as in a collision cell experiment.[26,56] The rate of loss of polarization in an elastic collision (no change of rotational level) or of transfer of polarization to another level is governed by tensor cross sections, which are generalizations of ordinary integral cross sections. The tensor cross section of rank K for a molecule in a $^2\Pi$ electronic state is given by the

following expression:[26,57,58]

$$\sigma_{jF\varepsilon \to j'F'\varepsilon'}^{(K)} = \frac{\pi}{k_{jF\varepsilon}^2} \sum_{\substack{J J' \\ l l'}} [J][J'] (-1)^{l+l'-j-j'+2J} \begin{Bmatrix} j & j & K \\ J & J' & l \end{Bmatrix}$$

$$\times \begin{Bmatrix} j' & j' & K \\ J & J' & l' \end{Bmatrix} T_{jF\varepsilon l, j'F'\varepsilon' l'}^{J} \left(T_{jF\varepsilon l, j'F'\varepsilon' l'}^{J'} \right)^*. \quad (2)$$

The rotational levels are specified by the rotational angular momentum j, the fine-structure manifold F [= F_1 or F_2, which correspond in the Hund's case (a) limit to $^2\Pi_{3/2}$ and $^2\Pi_{1/2}$, respectively, for CN($A^2\Pi$)],[59] and the symmetry index $\varepsilon = +1$ and -1 for e and f levels, respectively.[60] In Eq. (2), $k_{jF\varepsilon}$ is the wavevector of the initial level, $[x] = 2x + 1$, $\begin{Bmatrix} \bullet & \bullet & \bullet \\ \bullet & \bullet & \bullet \end{Bmatrix}$ is a 6j symbol,[61] J is the total angular momentum, l is the orbital (end-over-end) angular momentum of the triatomic complex, and the T quantities are T-matrix elements, expressed in a space-fixed frame.

The *loss* of polarization of rank K due to elastic collisions is described by an elastic depolarization cross section, which is the difference between the elastic tensor cross sections of ranks 0 and K:[26]

$$\sigma_{dep, jF\varepsilon}^{(K)} = \sigma_{jF\varepsilon \to jF\varepsilon}^{(K=0)} - \sigma_{jF\varepsilon \to jF\varepsilon}^{(K)}. \quad (3)$$

Loss of population of a given rotational level is determined by the sum of the state-to-state integral cross sections out of this level.[62]

Energy-dependent integral and tensor cross sections for the collision of CN($A^2\Pi$) with Ar were computed in a quantum mechanical treatment of the collision dynamics. Two sets of potential energy surfaces were employed in these calculations: the B-W PESs of Berning and Werner[32] and the new PESs described in Sec. II B.

Close-coupling calculations were carried out with the HIBRIDON suite of programs,[63] which was recently extended to include calculation of tensor cross sections for open-shell molecules.[26] Tests for the convergence of the cross sections were carried out to ensure inclusion of a sufficient number of both energetically closed and open channels and partial waves. It should be noted that the convergence requirements for elastic cross sections are greater than for inelastic cross sections. At the highest energies considered (2000 cm^{-1}), the rotational basis included all levels with $j \le 25.5$, and the scattering calculations included all total angular momenta $J \le 400.5$.

In order to compute thermal rate constants, the cross sections were calculated over a grid of collision energies, up to total energies of 2000 cm^{-1} and were averaged over a room-temperature ($T = 298$ K) Maxwellian distribution of relative velocities.[64]

III. RESULTS

A. Experimental results

The strongly saturating pump pulse used could, in principle, lead to the generation of orientation and alignment moments in the prepared level of rank $K \ge 2$. However, the one-photon linear probe used is only sensitive to mo-

ments of rank $K = 0$, 1, and 2,[65] and, as noted earlier, in the isotropic collision environment moments of different rank cannot mix.[66] Optical excitation also imposes cylindrical symmetry upon the prepared distribution. With a linear polarized pump, the observed signal is thus dependent on a population, $A_0^{(0)}$, and an alignment, $A_0^{(2)}$. With a circular polarized pump, this becomes: population, $A_0^{(0)}$; orientation, $A_0^{(1)}$; and alignment $A_0^{(2)}$. The $A_0^{(1)}$ and $A_0^{(2)}$ moments have the conventional high-j limits of -1 and $+1$, and -1 and $+2$, respectively.[67] The probe sensitivity to $A_0^{(0)}$, $A_0^{(1)}$ and $A_0^{(2)}$ depends on both the spectroscopic branch used, and the relative polarizations of the pump and probe lasers. As described in Section II A, two sets of geometries were used for the alignment (∥ and ⊥), and orientation (*co* and *con*) experiments, respectively. The integral intensities of the signals observed in the different geometries, $I_\|$ and $I_\perp$, or I_{co} and I_{con}, are given in Eqs. (4)–(7).

$$I_\| = \frac{ES}{3(2j+1)} A_0^{(0)} \left[1 + h^{(2)}(j) A_0^{(2)} \right], \quad (4)$$

$$I_\perp = \frac{ES}{3(2j+1)} A_0^{(0)} \left[1 - \frac{h^{(2)}(j)}{2} A_0^{(2)} \right], \quad (5)$$

$$I_{co} = \frac{ES}{3(2j+1)} A_0^{(0)} \left[1 + \frac{3}{2} h^{(1)}(j) A_0^{(1)} - \frac{1}{2} h^{(2)}(j) A_0^{(2)} \right], \quad (6)$$

$$I_{con} = \frac{ES}{3(2j+1)} A_0^{(0)} \left[1 - \frac{3}{2} h^{(1)}(j) A_0^{(1)} - \frac{1}{2} h^{(2)}(j) A_0^{(2)} \right]. \quad (7)$$

Here E is a constant that contains the experimental sensitivity to parameters such as optical path length, absolute number density and detector response, S is the rotational line strength factor and $h^{(K)}(j)$ is the rotational branch sensitivity to the moment of rank K.[43,68]

The experimental data were analyzed as FM Doppler line shapes. The acquired FM background 2D arrays were first subtracted from the corresponding signal arrays, for each experimental geometry. These I & Q arrays were then rotated to yield pure stimulated emission (SE) and dispersion (D) arrays.[69] FM Doppler line shapes for sequential 10 ns averages of the SE and D signals for each of the two geometries were constructed, with the wavelength axis linearized using the acquired monitor etalon traces. For the linear pump polarization measurements, Gaussian Doppler profiles for the ∥ and ⊥ geometries, with integral areas given by Eqs. (4) and (5), were simulated from assumed $A_0^{(0)}$ and $A_0^{(2)}$ moments, together with an assumed translational temperature. These line shapes were then transformed into FM SE and D line shapes and simultaneously least-squares fitted, using the Levenberg-Marquardt (LM) method to optimize the moments and translational temperature, to the experimental FM line shapes. This resulted in time-dependent population and alignment kinetic traces, and the time dependence of the translational temperature, which were stored for further analysis.

The fitted translational temperature immediately after the pump pulse was typically found to be 350 ± 5 K, independent

of the collider pressure. This slight super-thermal temperature is thought to be the result of the unresolved hyperfine structure of the transitions, together with a small contribution from instrumental broadening.[70] The observed temperature then declines, typically reaching a minimum around 300 K before increasing again. This behavior has been observed before in similar experiments, and has a straightforward physical explanation.[71] Those CN radicals within the Maxwell-Boltzmann distribution that have a higher velocity necessarily collide at a higher frequency. Provided that the population removal cross section does not have a strong *negative* collision-energy dependence, then the faster moving CN radicals will be preferentially removed, resulting in the observed decrease in translational temperature. At later times, as a substantial fraction of the population in the observed level consists of molecules that have undergone multiple state-changing collisions, we observe an increase in the fitted temperature, consistent with evolution back to a fully thermalized Maxwell-Boltzmann distribution. As the observed variations in temperature are relatively small, we expect any effect on the measured rate constants to be negligible, in comparison with the other experimental uncertainties. As such we do not discuss these effects any further in this paper.

The circularly polarized geometries have opposite sensitivities to $A_0^{(1)}$, but equal sensitivities to $A_0^{(2)}$ (Eqs. (6) and (7)), and it is thus not possible to completely isolate the $A_0^{(1)}$ dependence of the signal. The experimental data were treated in the same fashion as those for linear polarizations, up to the formation of averaged FM SE and D Doppler profiles. Simulated SE and D line shapes were again least-squares fitted to these, but in this case the LM minimization was applied to the intensities I_{co} and I_{con}, as well as the translational temperature. The resulting time-dependent kinetic traces were used to form the quantity C, defined as[72]

$$C = \frac{I_{co} - I_{con}}{I_{co} + I_{con}} = \frac{3h^{(1)}(j)A_0^{(1)}}{2 - h^{(2)}(j)A_0^{(2)}}. \qquad (8)$$

The initial alignment generated in the linear pump experiments was typically $A_0^{(2)} \leq -0.3$. However, this is defined in a laboratory frame referenced to the electric vector of the pump light. The correct laboratory frame for $A_0^{(2)}$ in Eq. (8) is the pump laser quantization axis, which is either parallel or anti-parallel to the pump propagation direction. As a result, the alignment in Eq. (8) is multiplied by a factor of $-1/2$.[43] In the experiments reported here, the probe laser was tuned to R_1-branch transitions in absorption, corresponding to the P_1-branch transitions in stimulated emission. The pre-multiplier, $h^{(2)}(j) = -(j + 1)/(2j - 1)$, and hence the overall contribution of the alignment to the denominator of Eq. (8) is $<5\%$. We have therefore discounted the small correction introduced by this alignment moment in our analysis of the circular polarized data, and henceforth consider C as directly proportional to the orientation, $A_0^{(1)}$. We have similarly treated the denominator of Eq. (8), $I_{co} + I_{con}$, as proportional to the population, $A_0^{(0)}$.

Figure 3 shows typical FM SE Doppler profiles immediately (10 ns) after the pump pulse for the co- and counter-rotating geometries, together with their fits, for $j = 6.5\ F_1e$
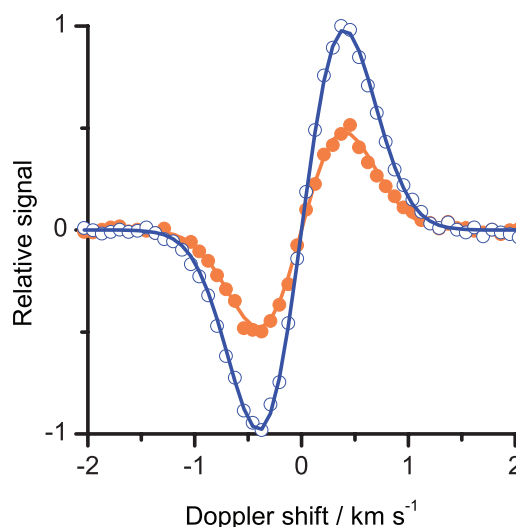

FIG. 3. FM stimulated emission Doppler profiles for $j = 6.5\ F_1e$ at 116 mTorr total pressure and 10 ns post-pump delay. Open circles: counter-rotating geometry; filled circles: co-rotating geometry, and solid lines: fits to I_{co} and I_{con}. Although not shown, the equivalent dispersion Doppler profiles were simultaneously fitted, as discussed in the text.

at a total pressure of 116 mTorr. The large difference between the two geometries clearly shows that a significant rotational orientation has been created by the pump pulse. Figure 4 shows the kinetic traces for I_{co} and I_{con} resulting from this Doppler profile analysis, for a total pressure of 116 mTorr for Fig. 4(a)(i) and 1000 mTorr for Fig. 4(b)(i). In both cases I_{con} is approximately twice the magnitude of I_{co} at $t = 0$, and both intensities decay with time as population is removed from the initial level by collisions. However, the two traces in each case *clearly converge*, indicating even by eye that collisional removal of the initial polarization is partially competitive with the loss of population. Comparison of the observed decay rates also shows clearly that they depend strongly on the collider pressure. In Figs. 4(a)(ii) and 4(b)(ii) these intensities have been converted into population, $I_{co} + I_{con}$, and the orientation parameter, C (Eq. (8)), suitable for further analysis. As expected the populations decay in a near exponential fashion with a rate dependent on pressure, although at long delay times the non-zero baseline is evidence of the thermalization of the initial population across the Boltzmann distribution within $A^2\Pi$ (v = 4). In contrast, the orientation decays much more slowly than the population, and while the decay clearly still depends on collider pressure, it is obviously not exponential. In each case the errors shown are 2σ from the LM minimization routine.

B. Quantum scattering results

Elastic tensor and depolarization cross sections for ranks $K = 1$ and 2 were computed for collisions of CN($A^2\Pi$, v = 4, $j = 1.5$–10.5, F_1e) rotational/fine-structure levels. In addition, integral cross sections for rotationally inelastic transitions out of these levels were computed and summed to yield total population transfer cross sections.

Figure 5 presents energy-dependent elastic depolarization cross sections [Eq. (3)] for several CN($A^2\Pi$) F_1e
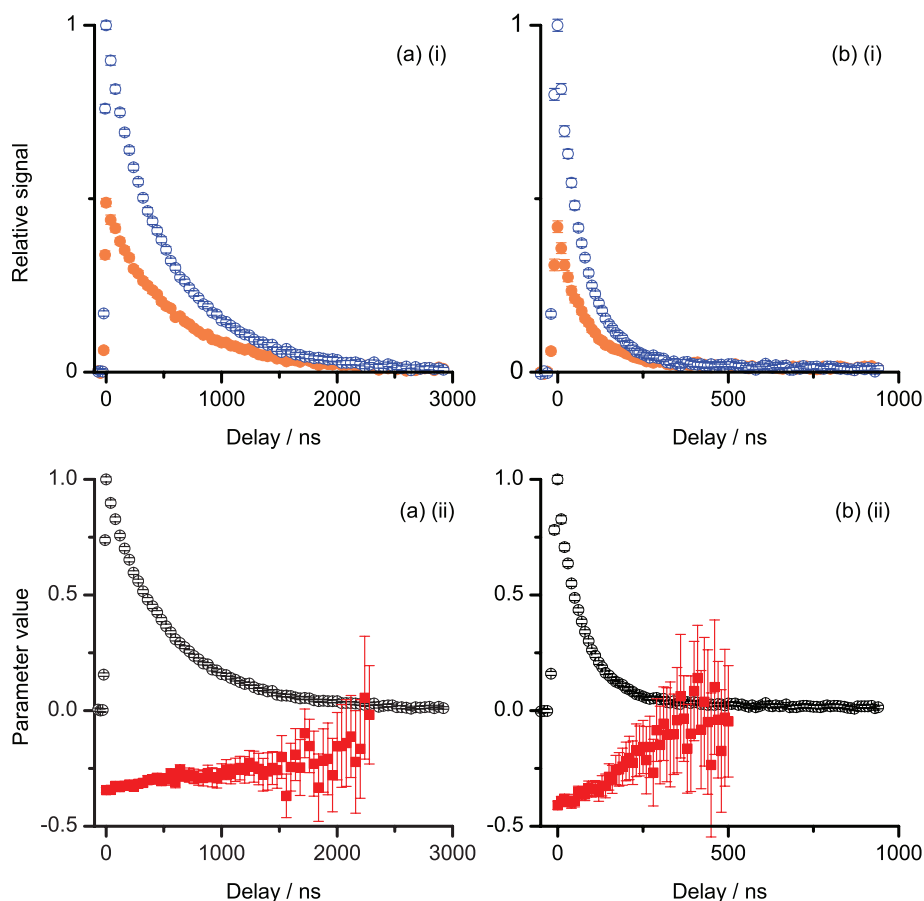
FIG. 4. Signal decays of I_{co} (filled circles) and I_{con} (open circles) for $j = 6.5$ F_1e (a)(i) at 116 mTorr total pressure and (b)(i) at 1000 mTorr. Relative population (open circles) and the orientation, C, (filled squares) derived from I_{co} and I_{con} (a)(ii) at 116 mTorr and (b)(ii) at 1000 mTorr. The error bars represent 2σ from the fits to the Doppler profiles. For the 1000 mTorr pressure every acquired data point is shown, for the 116 mTorr pressure every 4th point is shown.

rotational/fine-structure levels as a function of the incident relative translational energy in collisions with Ar. These cross sections were computed with the PESs determined in this work. Cross sections for the loss of orientation and alignment are displayed in Figs. 5(a) and 5(b), respectively. As found previously for collisions of OH($X^2\Pi$) and NO($X^2\Pi$) with Ar,[23,26] the $K = 2$ cross sections are larger than the $K = 1$ cross sections.

The elastic depolarization cross sections are seen in Fig. 5 to be very large at low collision energies and generally decrease with increasing collision energy, as was also found for NO($X^2\Pi$)–Ar collisions.[23] Sharp features in the energy-dependent cross sections are due to shape and Feshbach resonances and have been seen in the energy dependence of rotationally inelastic cross sections for scattering of other molecules.[27,73–75] The elastic depolarization cross sections displayed in Fig. 5 also decrease in magnitude with increasing j, as has been seen in other systems.[23,26,27]

Displayed in Fig. 6 are the energy-dependent total population removal cross sections $\sigma_{pop,j}$, i.e., namely the sum of the integral cross sections for all rotationally inelastic transitions out of the initial level. The individual state-to-state cross sections have been presented and discussed in previous publications,[32,39,76,77] and we do not consider them here. In behavior similar to that shown by the elastic depolarization

cross sections in Fig. 5, the total population removal cross sections generally decrease monotonically with increasing collision energy. Comparing Figs. 5 and 6, we see that population removal by rotational energy transfer is much more efficient than elastic depolarization. The total removal cross sections are seen to decrease in magnitude with increasing j, but the dependence upon j is much weaker than for elastic depolarization.

Energy-dependent cross sections such as those displayed in Figs. 5 and 6 were employed to determine the corresponding thermal rate constants $k_{pop,j}$. The rate constants for total population removal and $K = 1$ and 2 elastic depolarization for the $j = 1.5$–10.5 F_1e rotational/fine-structure levels, computed with the B-W (Ref. 32) and present PESs, are presented in Table I. The j dependence of the rate constants is similar to that observed for the energy-dependent cross sections. In addition, the elastic depolarization rate constants are much smaller than the total population removal rate constants. Comparing the rate constants computed with the two sets of PESs, we see that the total population removal rate constants computed with the present PESs are 11%–17% larger than those computed with the B-W PESs. With the exception of the rate constants for $j = 1.5$, which are significantly larger for the present PESs by $\sim$25%, the elastic depolarization rate constants are similar in magnitude for the two sets of PESs.
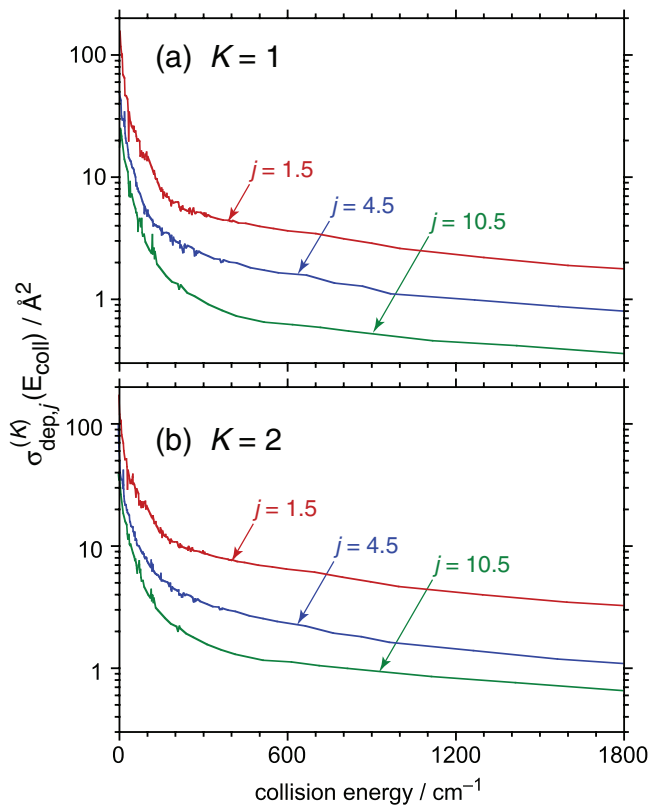
FIG. 5. Computed elastic depolarization cross sections for loss of (a) orientation [$K = 1$] and (b) alignment [$K = 2$] for the CN($A^2\Pi$, v = 4) $j = 1.5$, 4.5, and 10.5 $F_1 e$ rotational/fine-structure levels as a function of the incident relative translational energy in collisions with Ar.

IV. KINETICS OF POPULATION, ORIENTATION, AND ALIGNMENT DECAY

A. Master equation modeling

In order to investigate the effect of multiple collisions, we have carried out a complete kinetic simulation of the relaxation of the population and orientation of a selected initially prepared level, specifically the $j = 6.5$ $F_1 e$ level. As noted in Sec. II C and has been discussed in detail previously,[4,26] the
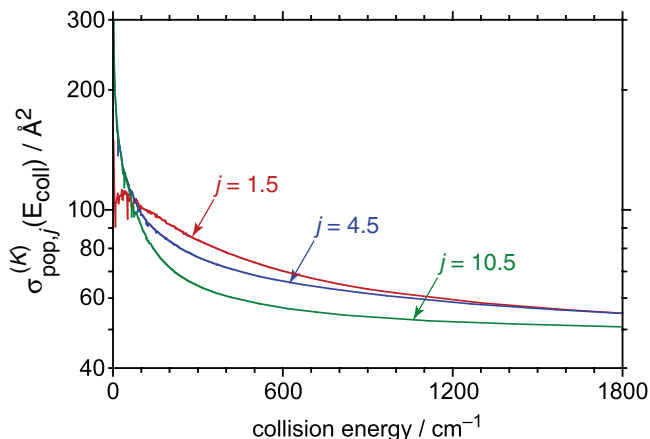

FIG. 6. Computed total population removal cross sections for the CN($A^2\Pi$, v = 4) $j = 1.5$, 4.5, and 10.5 $F_1 e$ rotational/fine-structure levels as a function of the incident relative translational energy in collisions with Ar.

TABLE I. Computed room-temperature rate constants (in units of 10^{-10} cm^3 s^{-1}) for elastic depolarization and removal of population by inelastic transitions for the CN($A^2\Pi$, v = 4) $j = 1.5$–10.5 $F_1 e$ levels in collisions with Ar.

	Berning-Werner PESs[a]			Present PESs		
j	$k_{pop,j}$	$k_{dep,i}^{(1)}$	$k_{dep,i}^{(2)}$	$k_{pop,j}$	$k_{dep,i}^{(1)}$	$k_{dep,i}^{(2)}$
1.5	4.44	0.327	0.583	5.19	0.422	0.724
2.5	4.50	0.308	0.429	5.24	0.274	0.391
3.5	4.39	0.254	0.347	5.07	0.226	0.335
4.5	4.28	0.183	0.278	4.90	0.189	0.288
5.5	4.17	0.152	0.245	4.73	0.157	0.251
6.5	4.10	0.128	0.220	4.60	0.132	0.220
7.5	4.04	0.113	0.201	4.51	0.113	0.194
8.5	3.98	0.101	0.183	4.43	0.101	0.175
9.5	3.92	0.096	0.173	4.36	0.095	0.164
10.5	3.87	0.093	0.164	4.29	0.093	0.158

[a]Reference 32.

state multipoles evolve independent of each other. The time evolution of the Kth state multipole $\rho^K(i)$ of the ith level is governed by the following equation:[26]

$$\frac{d}{dt}\rho^K(i) = -Nk_{pop,i}\rho^K(i)$$
$$-Nk_{dep,i}^{(K)}\rho^K(i) + N\sum_f k_{f\to i}^{(K)}\rho_{f\to i}^K. \quad (9)$$

Here, N is the number density of the collision partner, and $k_{f\to i}^{(K)}$ is the rate constant for collisional transfer of the rank K state multipole, respectively, from level f to level i. The first term on the RHS of Eq. (9) represents the loss of population (and hence polarization) by collisional transfer to other levels; the second term represents elastic depolarization of the level; and the last term represents collisional transfer of the state multipole back into the given level from other levels. For the $K = 0$ multipole (proportional to the population), Eq. (9) reduces to a simpler expression:

$$\frac{d}{dt}\rho^{K=0}(i) = -Nk_{pop,i}\rho^{K=0}(i) + N\sum_f k_{f\to i}^{(0)}\rho_{f\to i}^{K=0}. \quad (10)$$

Equation (10) is exactly analogous to the well-known equation[62] for the evolution of a level population; the $K = 0$ multipole has a different normalization than the population. It should be noted that the state-to-state $K = 0$ tensor rate constants are related to the state-to-state population transfer rate constants in the following way:[25,26,78]

$$k_{i\to f}^{(0)} = ([j_i]/[j_f])^{1/2}k_{i\to f}. \quad (11)$$

The relevant rate constants to simulate the relaxation of CN($A^2\Pi$) state multipoles were taken from the following sources. The elastic depolarization rate constants, $k_{dep,i}^{(K)}$, computed with the present potential, were taken from Table I. To facilitate the construction of the matrix of state-to-state population and tensor rate constants by avoiding the computational expense of computing many cross sections over a large grid of energies, a full thermal average of the state-to-state integral and tensor cross sections was not carried out. Rather, state-to-state cross sections for endothermic transitions were
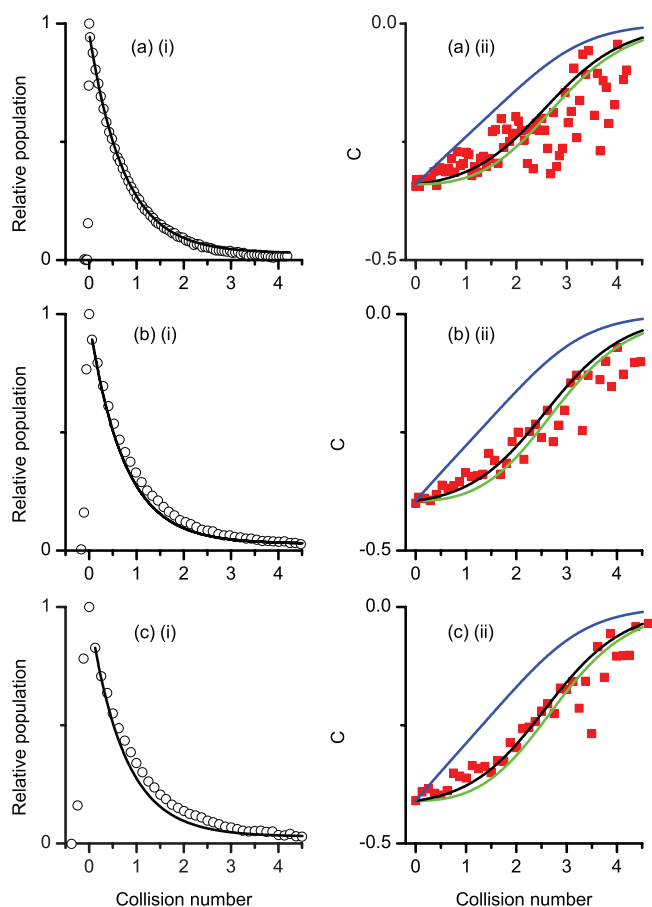
FIG. 7. Comparison of (i) measured population (open circles) and (ii) measured orientation ratio, C, (filled squares) for the CN(A$^2\Pi$, v = 4) $j = 6.5$ F_1e level to the master equation simulations (solid lines) for (a) 116 mTorr, (b) 465 mTorr, and (c) 1000 mTorr total pressures, as a function of collision number, calculated assuming $k = 3.9 \times 10^{-10}$ cm^3 s^{-1}. The black lines are the result of a simulation using the full QS rate constants, the green lines assume no elastic depolarization, and the blue lines assume all elastic depolarization rate constants have the value, $k_{dep}^{(K)} = 1 \times 10^{-10}$ cm^3 s^{-1}. In (c) all data points are shown, in (a) only every 4th point and in (b) only every 2nd point.

computed at a collision energy of 300 cm^{-1} and were assumed to be representative of the thermal average in order to determine the corresponding rate constants. The rate constants for the reverse exothermic transitions were computed by detailed balance. The population removal rate constants $k_{pop,j}$ were computed from appropriate sums of state-to-state rate constants.

The differential equations describing the time evolution of the state multipoles [Eqs. (9) and (10)] were solved through an analytic solution method described by Alexander *et al.*[62] Calculations were carried out with an Ar partial pressure of 200 mTorr; however, since all the rates scale with the Ar number density, these calculations can be scaled to any Ar pressure.

Figure 7 compares the time-dependent population and orientation of the $j = 6.5$ F_1e level measured at three different Ar pressures with the corresponding quantities computed in the kinetic simulation. The *x*-axes have been scaled to collision number, using the experimentally determined population removal rate constant (Subsection IV B). Orientation

was chosen for this comparison since the experimental sensitivity to orientation is higher than that of alignment (Eqs. (4)–(7)), although similar effects are observed for alignment. We see in Figs. 7(a)(i)–7(c)(i) that the time dependence of the population decay is reasonably well described by the simulation, although in each case the simulation decays slightly more rapidly than that observed experimentally. In addition, as there is no removal process from the A($^2\Pi$, v = 4) level in the simulation, the simulated population does not decay to zero, but rather to a Boltzmann distribution of populations. This leads to a non-zero long-time population in the initial level in the simulation, while the experiment sees slow removal of this Boltzmann distribution, presumably resulting from a combination of "fly-out" from the probe region, fluorescence,[79] and electronic and vibrational quenching.[77]

Figures 7(a)(ii)–7(c)(ii) compare the measured time-dependent orientation with several kinetic simulations. Simulations with the following assumptions about the elastic depolarization rate constants $k_{dep,j}^{(1)}$ were carried out: (1) using the rate constants obtained from the quantum scattering calculations (listed in Table I), (2) assuming that all $k_{dep,j}^{(1)}$ equal zero, and (3) assuming that all $k_{dep,j}^{(1)}$ equal 1×10^{-10} cm^3 s^{-1}, approximately the value determined for the $K = 2$ elastic depolarization rate constant for the $j = 6.5$ F_1e level in the previous work.[39] We see that in all cases the experimental data are not at all well fit by the assumption that $k_{dep,j}^{(1)}$ equal 1×10^{-10} cm^3 s^{-1}, which yields a much faster decay than is experimentally observed. Conversely, the assumption of no elastic depolarization predicts a somewhat slower decay of orientation than is seen experimentally. Of the above three assumptions, the rate constants determined in the quantum scattering calculations provide the best description of the experimentally observed decay of the orientation, although overall the observed decay is slightly faster than this full QS simulation.

It can be seen in Figs. 7(a)(ii)–7(c)(ii) that both the experimental and computed decay profiles of the orientation are decidedly non-exponential. The orientation is, of course, proportional to the ratio of the $K = 1$ to $K = 0$ multipoles, which each evolve independently, as discussed above. In the kinetic analysis by Ballingall *et al.*[39] it was assumed that all the state multipoles decay exponentially, at least for early times, and hence that the multipole ratio decays exponentially. This is equivalent to neglecting the back-transfer terms in Eqs. (10) and (11) [last terms on RHS]. We found from the simulations that this is a poor assumption, which the higher signal-to-noise orientation data presented here confirm. We have also compared the simulations of the population, $K = 0$ tensor moment with that of the $K = 1$ tensor moment. The simulated population decay was found to be much more non-exponential than that for the $K = 1$ tensor moment. This occurs for two reasons. First, the population decays to a non-zero value, while the orientation decays to zero at long time, since there can be no orientation at thermal equilibrium. Second, the back-transfer rate constants are larger for the population ($K = 0$) than for the orientation ($K = 1$), as the polarization is not perfectly preserved in each collision, i.e., there is substantial *inelastic* depolarization. This shows that when an experimental
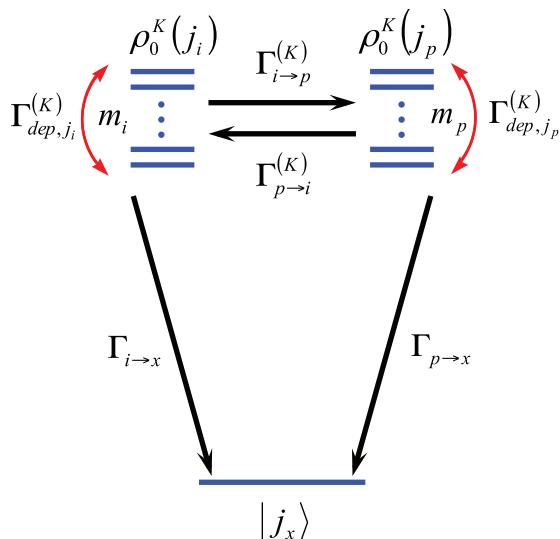
FIG. 8. The 3-level kinetic scheme discussed in the text, where the initial level is j_i, nearby product levels are j_p, with tensor moments $\rho_0^K(j_i)$ and $\rho_0^K(j_p)$, respectively, and the final unobserved level is j_x. $\Gamma_{i \to p}^{(K)}$ is a tensor-dependent transfer rate from level j_i to j_p, $\Gamma_{dep,j_i}^{(K)}$ is the tensor-dependent elastic depolarization rate for level j_i, and $\Gamma_{i \to x}$ is the total removal rate from level j_i to level j_x.

technique sensitive to the *tensor moments*, rather than the *normalized* orientation and alignment moments, is used, then the assumption of single exponential decay is generally valid. This is the case in the previous published PS experiments discussed in the Introduction.[4, 16–21, 23, 41]

B. Three-level kinetic fitting

The master equation modeling discussed in Sec. IV A clearly shows the importance of back-transfer in determining the forms of the observed population, and in particular, orientation or alignment moment kinetics. The simplest model that includes the effect of back-transfer in a physically reasonable fashion involves 3 distinct levels, as shown in Fig. 8. The first is the observed spectroscopic level, j_i. The second, j_p, represents close-lying rotational levels from which back-transfer to j_i is possible. Finally, j_x, represents those levels that are either far enough away (e.g., in energy, angular momentum, or even vibrational or electronic state), that back-transfer is effectively impossible. The rates for the transfer processes between j_i and j_p depend on the tensor rank, $\Gamma_{i \to p}^{(K)}$ and $\Gamma_{p \to i}^{(K)}$, while those for total removal to j_x are independent of rank, $\Gamma_{i \to x}$, and $\Gamma_{p \to x}$. The other significant process is elastic depolarization, which may occur within either j_i or j_p, with the rate $\Gamma_{dep,j}^{(K)}$. The kinetics of population transfer in such a 3-level system have been published previously.[80] A similar analysis for collisions of formaldehyde has been carried out by Coy *et al.*[81] We can generalize the expression given in Ref. 80 for the time evolution of the population of the initial level to one for the time evolution of the tensor moments of the initial level. We therefore express the time dependence of a

tensor moment of rank K of the initial level, j_i, as

$$\rho_0^K(j_i;t) = \frac{\rho_0^K(j_i;t=0)}{(\lambda_1^{(K)} - \lambda_2^{(K)})} \Big[(\Gamma_{i,tot}^{(K)} + \lambda_1^{(K)}) e^{\lambda_2^{(K)}t} - (\Gamma_{i,tot}^{(K)} + \lambda_2^{(K)}) e^{\lambda_1^{(K)}t} \Big]. \tag{12}$$

Since the $K = 0$ tensor moment is directly proportional to the population, we can express the time dependence of this tensor moment as

$$A_0^{(0)}(j_i;t) = \frac{A_0^{(0)}(j_i;t=0)}{(\lambda_1^{(0)} - \lambda_2^{(0)})} \Big[(\Gamma_{i,tot}^{(0)} + \lambda_1^{(0)}) e^{\lambda_2^{(0)}t} - (\Gamma_{i,tot}^{(0)} + \lambda_2^{(0)}) e^{\lambda_1^{(0)}t} \Big]. \tag{13}$$

Here $\Gamma_{i,tot}^{(0)}$ and $\Gamma_{p,tot}^{(0)}$, are the total population removal rates and may be expressed in our model as the sums of the individual population-transfer rates

$$\begin{aligned} \Gamma_{i,tot}^{(0)} &= \Gamma_{i \to p}^{(0)} + \Gamma_{i \to x}^{(0)}, \\ \Gamma_{p,tot}^{(0)} &= \Gamma_{p \to i}^{(0)} + \Gamma_{p \to x}^{(0)}. \end{aligned} \tag{14}$$

The parameters $\lambda_1^{(0)}$ and $\lambda_2^{(0)}$ have the forms

$$\begin{aligned} \lambda_1^{(0)} = -\frac{1}{2}\Big[\big[\Gamma_{i,tot}^{(0)} + \Gamma_{p,tot}^{(0)}\big] \\ - \sqrt{\big(\Gamma_{i,tot}^{(0)} - \Gamma_{p,tot}^{(0)}\big)^2 + 4\Gamma_{i \to p}^{(0)}\Gamma_{p \to i}^{(0)}} \Big], \\ \lambda_2^{(0)} = -\frac{1}{2}\Big[\big[\Gamma_{i,tot}^{(0)} + \Gamma_{p,tot}^{(0)}\big] \\ + \sqrt{\big(\Gamma_{i,tot}^{(0)} - \Gamma_{p,tot}^{(0)}\big)^2 + 4\Gamma_{i \to p}^{(0)}\Gamma_{p \to i}^{(0)}} \Big]. \end{aligned} \tag{15}$$

The orientation or alignment moments as conventionally defined are proportional to the relevant $K = 1$ or 2 tensor moment normalized by the $K = 0$ tensor moment.[67] The time dependence of the polarization of the initial state, $A_0^{(K)}(j_i)$, is thus

$$A_0^{(K)}(j_i;t) = A_0^{(K)}(j_i;t=0) \left[\frac{(\lambda_1^{(0)} - \lambda_2^{(0)})}{(\lambda_1^{(K)} - \lambda_2^{(K)})} \right] \times \frac{\big[(\Gamma_{i,tot}^{(K)} + \lambda_1^{(K)}) e^{\lambda_2^{(K)}t} - (\Gamma_{i,tot}^{(K)} + \lambda_2^{(K)}) e^{\lambda_1^{(K)}t}\big]}{\big[(\Gamma_{i,tot}^{(0)} + \lambda_1^{(0)}) e^{\lambda_2^{(0)}t} - (\Gamma_{i,tot}^{(0)} + \lambda_2^{(0)}) e^{\lambda_1^{(0)}t}\big]}. \tag{16}$$

Here $\Gamma_{i,tot}^{(0)}$ and $\Gamma_{p,tot}^{(0)}$, $\lambda_1^{(0)}$ and $\lambda_2^{(0)}$, are as defined in Eqs. (14) and (15). However, for tensors of rank $K \geq 1$ the elastic depolarization must be included as an additional loss process in the total removal rates

$$\begin{aligned} \Gamma_{i,tot}^{(K)} &= \Gamma_{i \to p}^{(0)} + \Gamma_{i \to x}^{(0)} + \Gamma_{dep,j_i}^{(K)}, \\ \Gamma_{p,tot}^{(K)} &= \Gamma_{p \to i}^{(0)} + \Gamma_{p \to x}^{(0)} + \Gamma_{dep,j_p}^{(K)}. \end{aligned} \tag{17}$$

Similarly, polarization may be lost in the transfer between j_i and j_p. It is convenient to include this by expressing the tensor transfer rates, $\Gamma_{i \to p}^{(K)}$ and $\Gamma_{p \to i}^{(K)}$, in terms of multipole transfer efficiencies.[4, 40]

$$\begin{aligned} \Gamma_{i \to p}^{(K)} &= \Gamma_{i \to p}^{(0)} E^{(K)}(j_i, j_p), \\ \Gamma_{p \to i}^{(K)} &= \Gamma_{p \to i}^{(0)} E^{(K)}(j_p, j_i). \end{aligned} \tag{18}$$
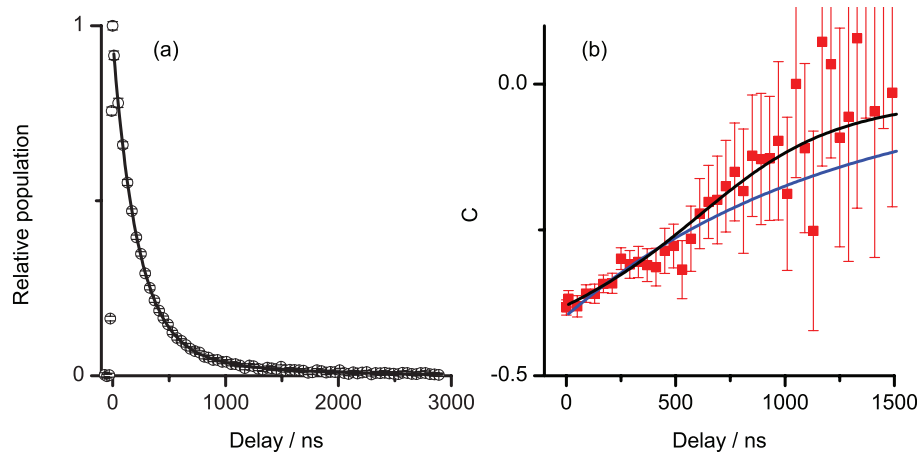
FIG. 9. (a) Measured relative populations (open circles) and (b) orientation parameter, C, (filled squares) for $j = 6.5$ $F_1 e$ at 291 mTorr total pressure, with every 4th point shown. The solid lines are fits from the 3-level kinetic model described in the text, assuming different average values for the orientation multipole transfer efficiency. Black line $\langle E^{(1)}(j, j') \rangle = 0.5$ and blue line $\langle E^{(1)}(j, j') \rangle = 1$.

The coefficients $\lambda_1^{(K)}$ and $\lambda_2^{(K)}$ are then given by

$$\lambda_1^{(K)} = -\frac{1}{2}\left[\Gamma_{i,tot}^{(K)} + \Gamma_{p,tot}^{(K)}\right]$$

$$-\sqrt{\left(\Gamma_{i,tot}^{(K)} - \Gamma_{p,tot}^{(K)}\right)^2 + 4\Gamma_{i\to p}^{(0)} E^{(K)}(j_i, j_p)\Gamma_{p\to i}^{(0)} E^{(K)}(j_p, j_i)},$$

$$\lambda_2^{(K)} = -\frac{1}{2}\left[\Gamma_{i,tot}^{(K)} + \Gamma_{p,tot}^{(K)}\right]$$

$$+\sqrt{\left(\Gamma_{i,tot}^{(K)} - \Gamma_{p,tot}^{(K)}\right)^2 + 4\Gamma_{i\to p}^{(0)} E^{(K)}(j_i, j_p)\Gamma_{p\to i}^{(0)} E^{(K)}(j_p, j_i)}. \tag{19}$$

We therefore have expressions for the time dependence of the population, and orientation or alignment, which can be fitted to the experimental data. We have also chosen to introduce some additional constraints on the rates in the above expressions. The removal rate to the final level, j_x, should not depend sensitively on the identity of j_i or j_p, so we have applied the constraint

$$\Gamma_{i\to x} = \Gamma_{p\to x}. \tag{20}$$

Although we expect the elastic depolarization rate to display some dependence on rotational level, as indeed predicted theoretically here (see Table I), we do not expect this variation with j to be sufficiently rapid to strongly influence the values of the other fitted parameters. We have therefore also applied the constraint

$$\Gamma_{dep, j_i}^{(K)} = \Gamma_{dep, j_p}^{(K)} = \left\langle\Gamma_{dep}^{(K)}\right\rangle. \tag{21}$$

Finally, as j_p represents a range of relatively nearby rotational levels, we have applied a single average MTE for population transfer in both directions

$$E^{(K)}(j_i, j_p) = E^{(K)}(j_p, j_i) = \left\langle E^{(K)}(j, j')\right\rangle. \tag{22}$$

We have performed fits to the experimental data using this model in the following fashion. We first fit the population kinetic trace to Eq. (13), varying the initial population, $A_0^{(0)}(j_i; t = 0)$, and the three rates $\Gamma_{i\to x} = \Gamma_{p\to x}$, $\Gamma_{i\to p}^{(0)}$, and $\Gamma_{p\to i}^{(0)}$. This yields the total population removal rate for the

initial level, $\Gamma_{i,tot}^{(0)}$ as defined in Eq. (14). These population rates were then fixed in the fitting of the orientation or alignment kinetic trace to Eq. (16), where we varied the initial orientation or alignment, $A_0^{(K)}(j_i; t = 0)$, and the elastic depolarization rate $\langle\Gamma_{dep}^{(K)}\rangle$. Trial fitting showed strong correlations between the elastic depolarization and MTE for any single kinetic trace, and we therefore held the average MTE at a preselected constant value in the fits reported below. The fitting was performed using a LM minimization by custom-written LabView® routines, with the data weighted by the previously determined errors. The fits were started 10 ns after the peak population, to avoid overlap with the pump pulse. The full range of acquisition times was used when fitting the population; for the orientation or alignment the fit was truncated to only include times where the population was larger than 1% of the initial value, and hence to exclude times where the polarization was ill determined.

Figure 9 shows the result of this fitting procedure applied to the population and orientation data for a single representative pressure (291 mTorr) for $j = 6.5$ $F_1 e$, with two different assumed values of the average MTE. The excellent fit to the population data, shown in Fig. 9(a), yields only statistical residual errors. The two different fits to the orientation data, shown in Fig. 9(b) [necessarily using the same population rates from Fig. 9(a)] are the result of fixing the MTE, $\langle E^{(1)}(j, j')\rangle$, to values of 0.5 and 1.0, respectively. The curve for $\langle E^{(1)}(j, j')\rangle = 1.0$ is clearly a considerably poorer fit, and in particular, fails to reproduce the observed multiple curvature of the data, also seen in the master equation simulations (recall Fig. 7). Analysis of Eqs. (12)–(22) shows that with this constraint the model results in the polarization displaying single-exponential decay kinetics. This is consistent with the shape of the relevant fitted curve shown in Fig. 9(b), and under these conditions the model is equivalent to that applied to the alignment depolarization in our previous work.[39] In addition to the failure of the fit, we know from the MTE values for $K = 2$ reported in Ref. 39, which range from 0.3 to 0.55, that substantial inelastic depolarization does occur. Trial fits to
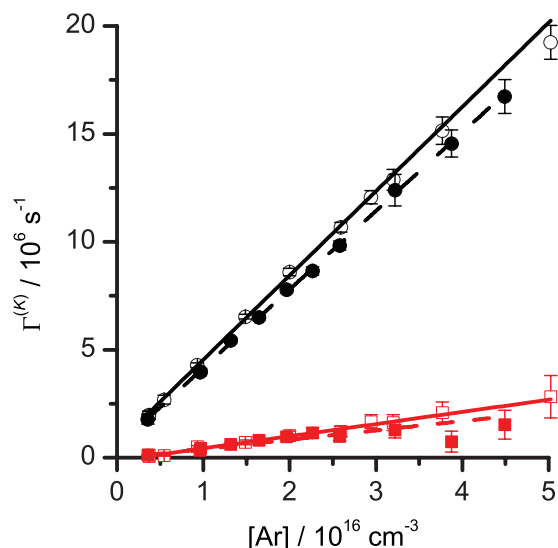
FIG. 10. Plots of the total population removal rate (circles), $\Gamma_{i,tot}^{(0)}$, and orientation elastic depolarization rate (squares), $\Gamma_{dep,j}^{(1)}$, for $j = 6.5$ $F_1 e$ (open symbols) and $j = 11.5$ $F_1 e$ (filled symbols) as a function of the collider number density. The rates were determined from the fits to the 3-level kinetic model described in the text. Lines (solid: $j = 6.5$; dashed: $j = 11.5$) are the result of linear least-squares weighted fits to determine the bimolecular rate constants.
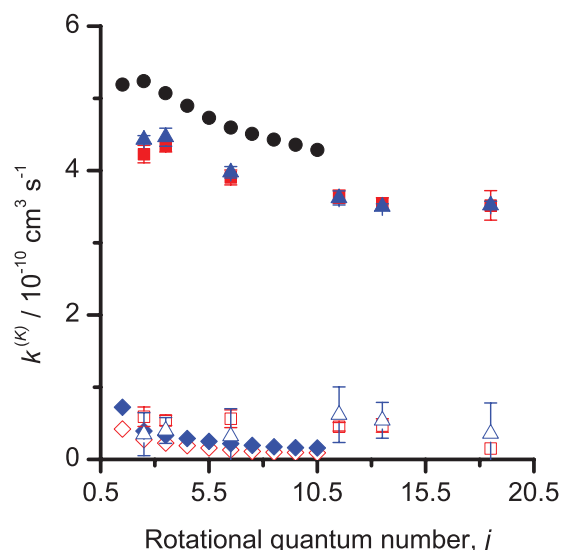
FIG. 11. Comparison of the experimentally determined population removal, k_{pop}, and elastic depolarization, $k_{dep}^{(K)}$, rate constants with those calculated according to Secs. II B and II C of this paper, on the present PESs. Filled circles: calculated population; filled squares: experimental population (from orientation measurements); and filled triangles: experimental population (from alignment measurements). Open diamonds: calculated orientation depolarization and open squares: experimental orientation depolarization. Filled diamonds: calculated alignment depolarization and open triangles: experimental alignment depolarization.

the orientation data for $j = 6.5$ $F_1 e$ across the range of pressures studied confirmed that the best overall fit quality was obtained with $\langle E^{(1)}(j, j')\rangle$ in the region of 0.5. This value was therefore used in all of the subsequent fitting to the orientation data, and the average value of the alignment MTE, $\langle E^{(2)}(j, j')\rangle = 0.44$, reported in Ref. 39, was used in fitting to the alignment measurements.

For each level studied ($j = 2.5, 3.5, 6.5, 11.5, 13.5,$ and 18.5), and for both the orientation and alignment data, the total removal rate of the initial level, $\Gamma_{i,tot}^{(0)}$, and the elastic depolarization rate, $\Gamma_{dep}^{(K)}$, were determined from these fits for each collider pressure, together with the 2σ statistical uncertainties arising from the LM fit to the 3-level model. Figure 10 shows example plots of the population and orientation removal rates for two rotational levels as a function of Ar pressure, together with weighted linear least-squares fits to extract the bimolecular rate constants, k_{pop,j_i} and $k_{dep,j_i}^{(K)}$. Finally, Table II summarizes these measured rate constants and the associated 2σ statistical uncertainties from the weighted linear fits, and Fig. 11 compares them to the theoretical predictions from our QS calculations. The orientation and alignment experiments provide independent measurements of the population removal rate constants, and are found to agree quantitatively with each other for all j. This supports our assumption to ignore the small alignment contribution to the orientation measurements explained in the context of Eq. (8). However, Fig. 11 also shows that the QS calculations systematically over-predict the measured k_{pop,j_i}, by approximately 15%. This is well outside the estimated 2σ uncertainties of the experiments. The elastic depolarization rate constants for orientation and alignment are found to lie in the range $(0–5) \times 10^{-11}$ cm^3 s^{-1}, with no obvious correlation with j or K. The uncertainties in these measurements are considerably larger

than in the corresponding populations, reflecting both the difficulty in measuring a slow process in the presence of much faster one (population removal), and the additional complication of the inelastic depolarization. However, they are much smaller than the previously reported alignment depolarization rate constants,[39] derived from fits to the (now clearly too simplistic) single exponential model, which are superseded by those presented here. In comparison to the calculated $k_{dep,j_i}^{(K)}$, good agreement is observed for the lowest rotational levels reported, $j = 2.5$ and 3.5, while at higher j the predicted values decline more rapidly than the measurements.

V. DISCUSSION AND CONCLUSIONS

We first discuss the total population removal rate constants. From Fig. 11, it is clear that the population removal

TABLE II. Experimentally determined rate constants (in units of 10^{-10} cm^3 s^{-1}) and 2σ statistical uncertainties for the total removal of population, $k_{pop,j}$, elastic depolarization of orientation, $k_{dep,j}^{(1)}$, and elastic depolarization of alignment, $k_{dep,j}^{(2)}$.

j	$k_{pop,j}$[a]	$k_{pop,j}$[b]	$k_{dep,j}^{(1)}$	$k_{dep,j}^{(2)}$
2.5	4.23 ± 0.12	4.43 ± 0.06	0.59 ± 0.14	0.35 ± 0.30
3.5	4.35 ± 0.09	4.46 ± 0.13	0.54 ± 0.07	0.40 ± 0.18
6.5	3.90 ± 0.10	3.98 ± 0.08	0.56 ± 0.12	0.32 ± 0.38
11.5	3.64 ± 0.09	3.62 ± 0.10	0.45 ± 0.06	0.62 ± 0.38
13.5	3.55 ± 0.08	3.50 ± 0.04	0.47 ± 0.09	0.54 ± 0.25
18.5	3.52 ± 0.20	3.52 ± 0.06	0.15 ± 0.28	0.36 ± 0.42

[a]Determined from measurements using circular polarization of pump and probe lasers.
[b]Determined from measurements using linear polarization of pump and probe lasers.

rate constants determined from fitting the data using the 3-level model are the same, within experimental precision, for the independent orientation and alignment measurements. They are slightly larger than the previously reported experimental rate constants, typically by 5%–10%.[39] This is consistent with a slight underestimation of the rate constants arising from neglect of the back-transfer in that work by fitting to a single exponential decay model. A similar 5%–10% difference is observed when the single exponential decay model is applied to the current data. For this reason, and the improved time resolution in the experiments reported here, we believe the current measurements are more reliable. Comparing the current experimental results to the QS calculations, very good agreement is found between experiment and the older B-W PESs, but the new PESs reported here predict population-removal rate constants that are consistently 10%–15% larger than experiment. The comparison of the master equation simulations using the QS results on the new PESs to the experimental data (Fig. 7) confirms that this slight over-prediction of the total removal rate constants is independent of any assumptions in the 3-level fitting. The level of agreement between experiment and theory is, in fact, much better than that which we found previously for the NO($X^2\Pi$)-Ar system.[23]

The major difference between the B-W PES and that reported here is the substantially deeper attractive well in the new PESs. As is shown in Fig. 6, the total population removal cross section displays a negative collision energy dependence, consistent with the attractive well playing a significant role. An appreciation of the lower-limit on the effective collision radius that must contribute to the population removal can be made by making the (unphysical) limiting assumption that the transition probability is unity out to some finite R, and zero thereafter. Converting the experimental rate constant into a thermally averaged cross section (for $j = 6.5$) gives $R = 8.5$ bohr, extending significantly into the attractive well of the PES. Clearly when considering a realistic R-dependence to the transition probability, this implies that collisions at even larger R are contributing to the total removal cross section. Although this might seem surprising for RET, such weak interactions have been previously shown to cause efficient pure-Λ doublet transfer in the OH($X^2\Pi$)–Ar system.[26] The presence of the deeper attractive well of the new PESs is strongly supported by the van der Waals complex spectroscopy of Heaven and co-workers.[34, 35] It therefore appears that the very good agreement between the calculations on the B-W PESs and the experiments is fortuitous, whilst the slight over-prediction of population transfer on the new PESs demonstrates that even this highly averaged quantity is remarkably sensitive to the PES.

Turning to the collisional depolarization, our primary experimental observation here is that the initially prepared orientation and alignment decay *non-exponentially*. This is therefore inconsistent with elastic depolarization being the only contributing collisional mechanism. This immediately suggests that *inelastic multiple-collisional depolarization* is a major contributor to the observed orientation and alignment decay of the initially prepared level. This is confirmed by the comparison of the master equation simulations to the experimental decays in Fig. 7. The general shape of the decays

is actually quite well reproduced by simulations in which only inelastic depolarization is allowed, while simulations with rapid elastic depolarization (as is a consequence of the assumptions in the previous work by Ballingall *et al.*[39]) are strikingly different to the experiments. The majority of the observed depolarization in these experiments is therefore due to inelastic collisions. We emphasize the general importance of considering such processes in measurements that are sensitive to all molecules in the quantum state, whether anisotropically polarized or not. The closest agreement between simulation and experiment is found using the elastic depolarization rate constants from the QS calculations, clearly indicating that the calculations give a good representation of the collisional depolarization, both elastic and inelastic. Closer inspection of the data and simulation show discrepancies at low collisional number, where we might expect the elastic depolarization to be the dominant process. Here the experimental polarization decay is consistently slightly faster than the simulation. Fitting of the 3-level kinetic model to the experimental data accordingly results in elastic depolarization rate constants that are generally somewhat larger than the QS calculations, albeit with a considerable degree of scatter that reflects the difficulty of extracting the rate constant for such a slow process when in competition with the rapid total population loss. However, we emphasize that despite these minor differences, the overall level of agreement between experiment and theory is generally good, and significantly, that this confirms that contrary to the conclusions of the previously published experiments,[39] elastic depolarization is a relatively minor channel in CN($A^2\Pi$) + Ar collisions.

The major difference in the QS results on the current and previous PESs is in the total population removal, noted above. The elastic depolarization rate constants are very similar except for detailed changes. The two sets of PESs may be compared by inspecting the contour plots of V_{sum} and V_{diff} presented in Fig. 2 and in Fig. S1 of the supplementary material. It can be seen that the largest difference is in the attractive region of the V_{sum} PESs, with the present potential showing a deepening of the attractive well. The anisotropy and range of the repulsive wall in V_{sum} are quite similar for the two potentials. The anisotropy and range of V_{diff} are also very similar for the two potentials. Comparison of the angular expansion coefficients for V_{sum} and V_{diff} for the two potentials, displayed in Figs. S2 and S3 in the supplementary material, confirms that the largest difference is in the isotropic term V_{00}, with a deeper attractive well for the present potential. This purely isotropic component of the PES cannot in itself induce a torque, and hence cannot directly cause either elastic depolarization or RET. However, it will have an influence on what parts of the PESs are sampled by collisions at particular collision energies and may therefore have a more subtle second-order effect on the overall scattering cross section and product branching.

The weak elastic depolarization observed here in CN($A^2\Pi$) + Ar is strikingly similar to that recently calculated and observed in the kinematically and energetically similar NO($X^2\Pi$) + Ar system.[23] This is notably distinct from the more rapid depolarization seen in the OH($X^2\Pi$) + Ar system,[20, 26] and very much slower than that observed in the strongly attractive OH($A^2\Sigma^+$) + Ar system.[16, 30] One possible

explanation for this contrast between systems is the effect of the rotor kinematics on the balance between elastic depolarization and population transfer.[5] The light OH rotor has large rotational spacings that hinder RET, while re-orientation of the H-atom towards the collider is relatively facile, as is observed in the QCT calculations by Brouard and co-workers on the OH($A^2\Sigma^+$) + Ar system.[30] In contrast, for NO and CN, the relatively heavy rotor is both harder to reorient classically, and also has much smaller rotational spacings, resulting in a bias towards RET.

Looking forward, in conclusion, the balance between kinematics and potential effects noted above could of course be explored via scattering calculations on hypothetical systems with artificially adjusted masses. On the experimental side, it would be interesting to explore the effect of more strongly interacting colliders, particularly those that might be expected to form collision complexes. The depolarization observed in collisions with Ar has been shown here to be dominated by inelastic scattering, and we expect that experimental measurements of the MTE for these transitions and associated QS calculations will provide additional novel insights into the dynamics.

[1] P. J. Dagdigian, in *Chemical Dynamics and Kinetics of Small Free Radicals*, edited by K. Liu and A. Wagner (World Science, Singapore, 1995), p. 315.

[2] A. Schiffman and D. W. Chandler, Int. Rev. Phys. Chem. **14**, 371 (1995).

[3] M. L. Costen, S. Marinakis, and K. G. McKendrick, Chem. Soc. Rev. **37**, 732 (2008).

[4] G. Paterson, M. L. Costen, and K. G. McKendrick, Mol. Phys. **109**, 2565 (2011).

[5] G. Paterson, M. L. Costen, and K. G. McKendrick, Int. Rev. Phys. Chem. **31**, 69 (2012).

[6] N. A. Jackson, C. J. Randall, and K. G. McKendrick, Chem. Phys. **233**, 45 (1998).

[7] E. A. Brinkman and D. R. Crosley, J. Phys. Chem. A **108**, 8084 (2004).

[8] S. J. Silvers, R. A. Gottscho, and R. W. Field, J. Chem. Phys. **74**, 6000 (1981).

[9] A. D. Rudert, J. Martin, W. B. Gao, H. Zacharias, and J. B. Halpern, J. Chem. Phys. **112**, 9749 (2000).

[10] A. D. Rudert, J. Martin, W. B. Gao, J. B. Halpern, and H. Zacharias, J. Chem. Phys. **111**, 9549 (1999).

[11] J. B. Halpern, R. Dopheide, and H. Zacharias, J. Phys. Chem. A **99**, 13611 (1995).

[12] H. J. Crichton, M. L. Costen, and K. G. McKendrick, J. Chem. Phys. **119**, 9461 (2003).

[13] M. L. Costen, H. J. Crichton, and K. G. McKendrick, J. Chem. Phys. **120**, 7910 (2004).

[14] M. L. Costen and K. G. McKendrick, J. Chem. Phys. **122**, 164309 (2005).

[15] M. Brouard, A. Bryant, I. Burak, S. Marinakis, F. Quadrini, I. A. Garcia, and C. Vallance, Mol. Phys. **103**, 1693 (2005).

[16] M. L. Costen, R. Livingstone, K. G. McKendrick, G. Paterson, M. Brouard, H. Chadwick, Y. P. Chang, C. J. Eyles, F. J. Aoiz, and J. Kłos, J. Phys. Chem. A **113**, 15156 (2009).

[17] S. Marinakis, G. Paterson, J. Kłos, M. L. Costen, and K. G. McKendrick, Phys. Chem. Chem. Phys. **9**, 4414 (2007).

[18] G. Paterson, S. Marinakis, M. L. Costen, and K. G. McKendrick, Phys. Scr. **80**, 048111 (2009).

[19] G. Paterson, S. Marinakis, M. L. Costen, K. G. McKendrick, J. Kłos, and R. Toboła, J. Chem. Phys. **131**, 159901 (2009).

[20] G. Paterson, S. Marinakis, M. L. Costen, K. G. McKendrick, J. Kłos, and R. Toboła, J. Chem. Phys. **129**, 074304 (2008).

[21] G. Paterson, S. Marinakis, J. Kłos, M. L. Costen, and K. G. McKendrick, Phys. Chem. Chem. Phys. **11**, 8804 (2009).

[22] M. Brouard, A. Bryant, Y. P. Chang, R. Cireasa, C. J. Eyles, A. M. Green, S. Marinakis, F. J. Aoiz, and J. Kłos, J. Chem. Phys. **130**, 044306 (2009).

[23] G. Paterson, A. Relf, M. L. Costen, K. G. McKendrick, M. H. Alexander, and P. J. Dagdigian, J. Chem. Phys. **135**, 234304 (2011).

[24] M. Brouard, H. Chadwick, Y. P. Chang, R. Cireasa, C. J. Eyles, A. O. La Via, N. Screen, F. J. Aoiz, and J. Kłos, J. Chem. Phys. **131**, 104307 (2009).

[25] F. J. Aoiz, M. Brouard, C. J. Eyles, J. Kłos, and M. P. de Miranda, J. Chem. Phys. **130**, 044305 (2009).

[26] P. J. Dagdigian and M. H. Alexander, J. Chem. Phys. **130**, 094303 (2009).

[27] P. J. Dagdigian and M. H. Alexander, J. Chem. Phys. **130**, 164315 (2009).

[28] P. J. Dagdigian and M. H. Alexander, J. Chem. Phys. **130**, 204304 (2009).

[29] M. Brouard, H. Chadwick, C. J. Eyles, F. J. Aoiz, and J. Kłos, J. Chem. Phys. **135**, 084305 (2011).

[30] M. Brouard, H. Chadwick, Y. P. Chang, C. J. Eyles, F. J. Aoiz, and J. Kłos, J. Chem. Phys. **135**, 084306 (2011).

[31] X. Yang and P. J. Dagdigian, Chem. Phys. Lett. **297**, 506 (1998).

[32] M. H. Alexander, X. Yang, P. J. Dagdigian, A. Berning, and H. J. Werner, J. Chem. Phys. **112**, 781 (2000).

[33] X. Yang, P. J. Dagdigian, and M. H. Alexander, J. Chem. Phys. **112**, 4474 (2000).

[34] J. D. Han, M. C. Heaven, U. Schnupf, and M. H. Alexander, J. Chem. Phys. **128**, 104308 (2008).

[35] J. Han, M. C. Heaven, and U. Schnupf, J. Chem. Phys. **128**, 224309 (2008).

[36] A. Alagappan, I. Ballingall, M. L. Costen, and K. G. McKendrick, J. Chem. Phys. **126**, 041103 (2007).

[37] A. Alagappan, I. Ballingall, M. L. Costen, K. G. McKendrick, and G. Paterson, Phys. Chem. Chem. Phys. **9**, 747 (2007).

[38] A. Alagappan, M. L. Costen, and K. G. McKendrick, Spectrochim. Acta, Part A **63**, 910 (2006).

[39] I. Ballingall, M. F. Rutherford, K. G. McKendrick, and M. L. Costen, Mol. Phys. **108**, 847 (2010).

[40] M. H. Alexander and T. Orlikowski, J. Chem. Phys. **80**, 1506 (1984).

[41] S. Marinakis, G. Paterson, G. Richmond, M. Rockingham, M. L. Costen, and K. G. McKendrick, J. Chem. Phys. **128**, 021101 (2008).

[42] M. L. Costen, S. W. North, and G. E. Hall, J. Chem. Phys. **111**, 6735 (1999).

[43] M. L. Costen and G. E. Hall, Phys. Chem. Chem. Phys. **9**, 272 (2007).

[44] I. Nadler, D. Mahgerefteh, H. Reisler, and C. Wittig, J. Chem. Phys. **82**, 3885 (1985).

[45] R. A. Kendall, T. H. Dunning, and R. J. Harrison, J. Chem. Phys. **96**, 6796 (1992).

[46] D. E. Woon and T. H. Dunning, J. Chem. Phys. **98**, 1358 (1993).

[47] F. M. Tao and Y. K. Pan, J. Chem. Phys. **97**, 4989 (1992).

[48] M. H. Alexander, Chem. Phys. **92**, 337 (1985).

[49] P. J. Knowles, C. Hampel, and H. J. Werner, J. Chem. Phys. **99**, 5219 (1993).

[50] H.-J. Werner, P. J. Knowles, R. Lindh, F. R. Manby, M. Schütz *et al.*, MOLPRO, version 2006.3, a package of *ab initio* programs, 2006, see http://www.molpro.net.

[51] S. F. Boys and F. Bernardi, Mol. Phys. **19**, 553 (1970).

[52] T. S. Ho and H. Rabitz, J. Chem. Phys. **104**, 2584 (1996).

[53] T. Hollebeek, T. S. Ho, and H. Rabitz, Annu. Rev. Phys. Chem. **50**, 537 (1999).

[54] See supplementary material at http://dx.doi.org/10.1063/1.4705118 for contour plots of the B-W PESs and the angular expansion coefficients of the present and the B-W PESs.

[55] I. P. Hamilton and J. C. Light, J. Chem. Phys. **84**, 306 (1986).

[56] B. Follmeg, P. Rosmus, and H. J. Werner, J. Chem. Phys. **93**, 4687 (1990).

[57] M. D. Rowe and A. J. Mccaffery, Chem. Phys. **43**, 35 (1979).

[58] M. H. Alexander and S. L. Davis, J. Chem. Phys. **78**, 6754 (1983).

[59] G. Herzberg, *Molecular Spectra and Molecular Structure I. Spectra of Diatomic Molecules*, 2nd ed. (Van Nostrand, Princeton, 1950).

[60] J. M. Brown, J. T. Hougen, K.-P. Huber, J. W. C. Johns, I. Kopp, H. Lefebvre-Brion, A. J. Merer, D. A. Ramsay, J. Rostas, and R. N. Zare, J. Mol. Spectrosc. **55**, 500 (1975).

[61] R. N. Zare, *Angular Momentum* (Wiley, New York, 1988).

[62] M. H. Alexander, G. E. Hall, and P. J. Dagdigian, J. Chem. Educ. **88**, 1538 (2011).

[63] HIBRIDON, a package of programs for the time-independent quantum treatment of inelastic collisions and photodissociation written by M. H. Alexander, D. E. Manolopoulos, H.-J. Werner, B. Follmeg, and P. J. Dagdigian, with contributions from D. Lemoine, P. Vohralik, G. Corey, R. Johnson, T. Orlikwoski, A. Berning, A. Degli-Esposti, C. Rist, B. Pouilly, J. Kłos, Q. Ma, G. van der Sanden, M. Yang, F. de Weerd, S. Gregurick, and F. Lique, see http://www2.chem.umd.edu/groups/alexander/hibridon/hib43.

[64] I. W. M. Smith, *Kinetics and Dynamics of Elementary Gas Reactions* (Buttersworths, London, 1980).

[65] U. Fano and J. H. Macek, Rev. Mod. Phys. **45**, 553 (1973).

[66] K. Blum, *Density Matrix Theory and Applications*, 2nd ed. (Plenum, New York, 1996).

[67] A. J. Orr-Ewing and R. N. Zare, Annu. Rev. Phys. Chem. **45**, 315 (1994).

[68] R. Uberna, R. D. Hinchliffe, and J. I. Cline, J. Chem. Phys. **103**, 7934 (1995).

[69] S. W. North, X. S. Zheng, R. Fei, and G. E. Hall, J. Chem. Phys. **104**, 2129 (1996).

[70] M. L. Hause, G. E. Hall, and T. J. Sears, J. Mol. Spectrosc. **253**, 122 (2009).

[71] G. E. Hall, private communication (2010).

[72] A. J. Bain and A. J. Mccaffery, J. Chem. Phys. **83**, 2632 (1985).

[73] L. N. Smith, D. J. Malik, and D. Secrest, J. Chem. Phys. **71**, 4502 (1979).

[74] K. M. Christoffel and J. M. Bowman, J. Chem. Phys. **78**, 3952 (1983).

[75] P. J. Dagdigian and M. H. Alexander, J. Chem. Phys. **135**, 064306 (2011).

[76] N. Furio, A. Ali, and P. J. Dagdigian, J. Chem. Phys. **85**, 3860 (1986).

[77] J. H. Guo, A. Ali, and P. J. Dagdigian, J. Chem. Phys. **85**, 7098 (1986).

[78] M. P. de Miranda and D. C. Clary, J. Chem. Phys. **106**, 4509 (1997).

[79] Y. H. Huang, R. C. Lu, and J. B. Halpern, Appl. Opt. **32**, 981 (1993).

[80] C. J. Randall, C. Murray, and K. G. McKendrick, Phys. Chem. Chem. Phys. **2**, 461 (2000).

[81] S. L. Coy, S. D. Halle, J. L. Kinsey, and R. W. Field, J. Mol. Spectrosc. **153**, 340 (1992).